ANL/NE-16/12

Experimental studies of Micro- and Nano-grained UO_2: Grain Growth Behavior, Surface Morphology, and Fracture Toughness

Nuclear Engineering Division

ANL/NE-16/12

Experimental studies of Micro- and Nano-grained UO_2: Grain Growth Behavior, Surface Morphology, and Fracture Toughness

prepared by
Yinbin Miao, Kun Mo, Laura M. Jamison
Nuclear Engineering Division, Argonne National Laboratory

Jie Lian and Tiankai Yao
Rensselaer Polytechnic Institute

Sumit Bhattacharya
Materials Science Division, Argonne National Laboratory & Northwestern University

prepared for
U.S. Department of Energy
Nuclear Energy Advanced Modeling & Simulation Program

ABSTRACT

This activity is supported by the US Nuclear Energy Advanced Modeling and Simulation (NEAMS) Fuels Product Line (FPL) and aims at providing experimental data for the validation of the mesoscale simulation code MARMOT. MARMOT is a mesoscale multiphysics code that predicts the coevolution of microstructure and properties within reactor fuel during its lifetime in the reactor. It is an important component of the Moose-Bison-Marmot (MBM) code suite that has been developed by Idaho National Laboratory (INL) to enable next generation fuel performance modeling capability as part of the NEAMS Program FPL. In order to ensure the accuracy of the microstructure based materials models being developed within the MARMOT code, extensive validation efforts must be carried out. In this report, we summarize the experimental efforts in FY16 including the following important experiments: (1) in-situ grain growth measurement of nano-grained UO_2; (2) investigation of surface morphology in micro-grained UO_2; (3) Nano-indentation experiments on nano- and micro-grained UO_2. The highlight of this year is: we have successfully demonstrated our capability to in-situ measure grain size development while maintaining the stoichiometry of nano-grained UO_2 materials; the experiment is, for the first time, using synchrotron X-ray diffraction to in-situ measure grain growth behavior of UO_2.

CONTENTS

FIGURES

TABLES

1. Introduction

1.1 Brief Introduction to the MARMOT Simulation Code

MARMOT is a mesoscale multiphysics code that predicts the coevolution of microstructure and properties within reactor fuel during its lifetime in the reactor. It is an important component of the Moose-Bison-Marmot (MBM) code suite that has been developed by Idaho National Laboratory (INL) to enable next generation fuel performance modeling capability as part of the NEAMS Program Fuels Product Line (FPL). The BISON code is a main component of the MBM code suite to provide nuclear fuel performance modeling capabilities. Many of the materials models within the BISON fuel performance code are legacy materials models that are primarily empirical fits to experimental data. Although these materials models are well established and have been used for years, they cannot provide the predictive capability required in the next generation fuel performance code. Empirical models can hardly be extrapolated outside the bounds of experimental conditions, and therefore are not applicable to new reactor concepts or ultra-high burnup scenarios of existing reactor designs. In addition, these empirical models are usually correlated to burnup of the fuels. However, burnup is not a unique measure of fuel irradiation history, as fuels can reach the same burnup via different routes and therefore have very different microstructures and properties. Thus, models that are sensitive to microstructures of fuel materials are more ideal to be used in the next generation fuel performance code. To this end, the MARMOT code emphasizes the importance of modeling the fuel material behavior and properties with microstructure-based models.

1.2 The Objectives

In order to ensure the accuracy of the microstructure-based materials models being developed within the MARMOT code, extensive validation efforts must be carried out. In FY16, we have conducted several important experiments on UO_2 materials in different grain sizes (the main focus is on nano-grained UO_2). These studies/experiments include: (1) in-situ grain growth measurements of nano-grained UO_2 at Advanced Photon Source (APS) at Argonne National Laboratory (ANL); (2) synchrotron micro-diffraction and scanning electron microscopic characterizations for surface morphology of micro-grained UO_2; (3) Nano-indentation of micro- and nano-grained UO_2.

These proposed experiments are of both scientific and engineering significance. The first study: in-situ grain growth measurements of nano-grained UO_2 is to use, for the first time, synchrotron X-ray diffraction to in-situ characterize grain growth behavior of UO_2 materials. The success of the experiment demonstrated the feasibility of using high-energy, high-flux X-ray to in-situ measure the grain size development of nano-grained UO_2 samples. With the developed technique and experimental apparatus from this experiment, we can further apply different environments and temperatures onto UO_2 samples in different stoichiometry and porosities. Moreover, nano-grained UO_2 samples can be irradiated at Argonne Tandem Linac Accelerator System (ATLAS) to produce high-burnup Xe bubble structures. The irradiated sample with simulated high-burnup structures produced by the Xe implantations can be employed for further in-situ grain growth experiment. The second study is surface morphology characterization of micro-grained UO_2. Surface properties of UO_2 play an important role throughout the lifetime of this widely-used commercial nuclear fuel material, from manufacturing to storage. The surface features and corresponding thermodynamic characteristics influence the morphology, size, and distribution of fission gas bubbles as well as the initiation and propagation of micro-fractures within the nuclear fuel pellets. We collaboratively utilized synchrotron Laue microdiffraction and scanning electron microscopic techniques to establish a general correlation between the crystallographic orientation and surface faceting features of polycrystalline UO_2. The third study is fracture toughness measurements of micro- and nano-grained UO_2 materials. Previous experimental data for UO_2 materials are limited, particularly for nano-grained UO_2 materials. Sufficient amount of fracture toughness experimental data is necessary to validate the models and simulation performance of MARMOT code. Through crack length measurements, the fracture toughness was obtained for both micro- and nano-grained UO_2 samples.

1.3 The Structure and Content of This Report

In this report, we summarize our accomplishments in our experimental efforts in FY16. Three studies/experiments were individually described in each chapter.

The first chapter of this report introduces the background for this work and summarizes our major achievements.

Chapter 2 summarizes in-situ grain growth measurements on nano-grained UO_2 samples. This experiment is to use, for the first time, synchrotron X-ray diffraction, to in-situ characterize grain growth behavior of UO_2 samples. The nano-grained UO_2 samples were isothermally heated at two different temperatures, and in-situ characterized with high-energy synchrotron X-ray. The experimental setup, data interpretation methods, and procedures are given in detail in this chapter. Preliminary results interpreted from diffraction patterns were provided.

Chapter 3 summarizes the surface morphology study of a thermally etched UO_2 sample. Coordinated experimental efforts to quantitatively correlate crystallographic orientation and surface faceting features in UO_2 are reported in this chapter. A sintered polycrystalline UO_2 sample was thermally etched to induce the formation of surface faceting features. Synchrotron Laue microdiffraction was used to obtain a precise crystallographic orientation map for the UO_2 surface grains. Scanning electron microscopy (SEM) was utilized to collect the detailed information on the surface morphology of the sample. The surface faceting features were found to be highly dependent on the crystallographic orientation. In most cases, triple-plane structures containing one {100} plane and two {111} planes were found to dominate the surface of UO_2. The orientation-faceting relationship established in this study revealed a practical and efficient method of determining crystallographic orientation based on the surface features captured by SEM images.

Chapter 4 summarizes the fracture toughness measurements of micro- and nano-grained UO_2 samples. Through measuring the crack lengths produced by nano-indentation, the fracture toughness was obtained for the UO_2 samples in two different grain sizes. Fracture stress can be further determined based on the measured fracture toughness.

Chapter 5 outlines the planned experimental work for FY17. In FY16, We have completed a set of pilot experiments using synchrotron X-rays to in-situ analyze grain growth behavior of nano-grained UO_2. The success of experiments demonstrated the feasibility of applying synchrotron technique to yield real-time grain size as a function of annealing temperature. To complete a systematic study of grain growth behavior of nano-grained UO_2, we plan to study stoichiometric nano-crystalline UO_2 specimens at various temperatures. In addition, systematic studies for fracture toughness and stress of stoichiometric UO_2 samples in different grain sizes and microstructures will be conducted in FY17.

Finally, Chapter 6 provides a summary of the work conducted in this fiscal year.

2. In-situ Grain Growth Measurement of Nano-grained UO_2

In FY15, a preliminary synchrotron radiation experiment has been conducted to develop the methodology for grain size measurement of the nano-grained UO_2 samples. This preliminary synchrotron experiment was conducted at sector 1-ID at APS. The synchrotron experimental details, procedure for data analysis, and the results and discussion of the preliminary study of the nano-grained UO_2 have been reported in Ref. [1]. Due to the stringent safety regulation, the heating for UO_2 samples requires two-layers of containment for APS experiments, and the design of the container was not ready in FY15. In FY16, we had designed, tested and implemented a new apparatus to provide high vacuum, high temperature, and double containments for the UO_2 samples with in-situ X-ray characterizations capability. Using the apparatus, in-situ grain growth measurements of nano-grained UO_2 for two temperatures (730 ºC and 820 ºC) were conducted. The results of experiments were reported in the following sections.

2.1.1 Description of the sample

The nano-grained UO_2 samples were fabricated utilizing spark plasma sintering (SPS). Detailed fabrication procedure has been given in ref. [2]. The samples are in the dimensions of 2 mm × 2 mm × 0.45 mm. The stoichiometry of the nano-grained UO_2 samples was determined to be 2.006 ± 0.002 based on X-ray diffraction (XRD) pattern. The porosity is about 3.5% measured by SEM. Additionally, by measuring the SEM image as shown in Fig 2.1, the grain size was determined to be 120 ± 5 nm.

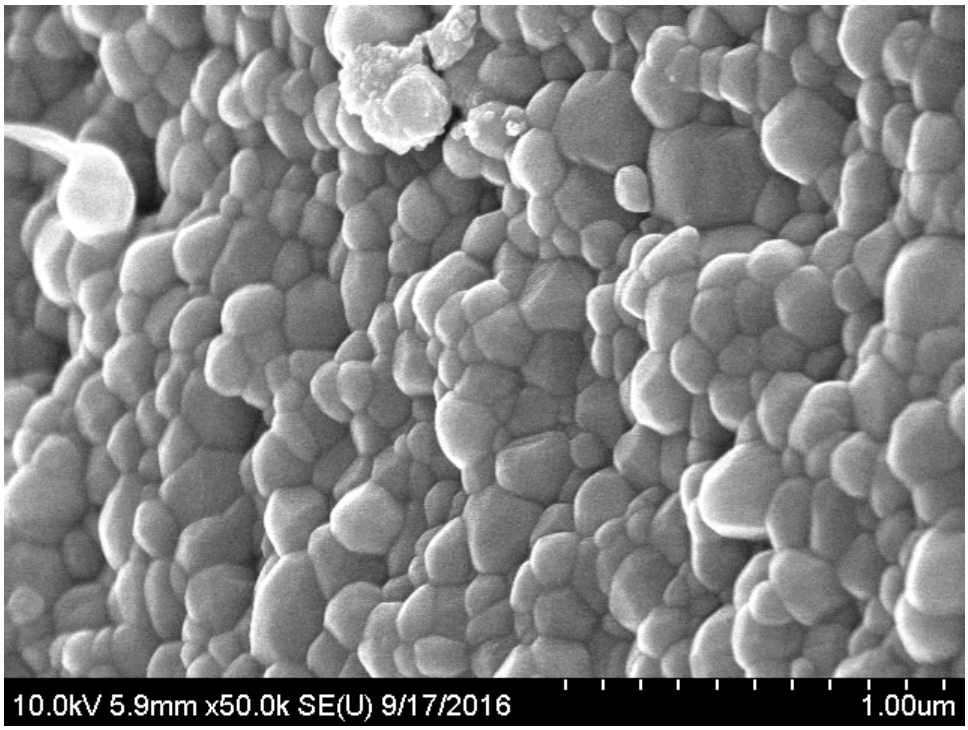

Figure 2.1: Fracture surface of the as-received nano-grained UO_2 sample

2.1.2 Experimental Setup and Sample Containment

In order to fulfill the requirements of radioactive materials regulations for APS experiments, a special apparatus was designed and installed in Sector 1-ID E Hutch at APS. Fig. 2.2 shows an apparatus for in-situ synchrotron characterization of nuclear fuel materials. The apparatus can be pumped to high

vacuum (up to 10^{-7} torr) and sealed with an all-metal valve. Vacuum level was monitored by a vacuum gauge during pumping and experiments. The apparatus can be operated in two modes: (1) pump to high-vacuum and maintained a reasonable vacuum level by closing the all-metal valve; the whole system is integrated, and no need to operate during the experiment; (2) keep the pumping system working during the experiment and then maintain a high-vacuum throughout the experiment. The first mode was used in this study.

The sintered nano-grained UO_2 samples were wrapped in double layers of ultra-thin (10 μm) nickel foils and fastened on the sample holder. The sample holder was then contained in a quartz vacuum dome. The upper part of the dome was heated externally by an infrared clamp furnace up to 730 °C and 820 °C, respectively. The temperature of the sample was controlled by one thermocouple and monitored by another three thermocouples inside the dome, while the vacuum of the dome will be measured by a standalone gauge. In addition, the actually sample temperature was deduced by the lattice constant measured by synchrotron diffraction based on the thermal expansion coefficient of UO_2 [3]:

$$\frac{\Delta a_0}{a_0} = \begin{cases} 9.973\times10^{-1} + 9.802\times10^{-6}T - 2.705\times10^{-10}T^2 + 4.391\times10^{-13}T^3, 273K\sim923K \\ 9.9672\times10^{-1} + 1.179\times10^{-5}T - 2.429\times10^{-9}T^2 + 1.219\times10^{-12}T^3, 923K\sim3120K \end{cases}$$

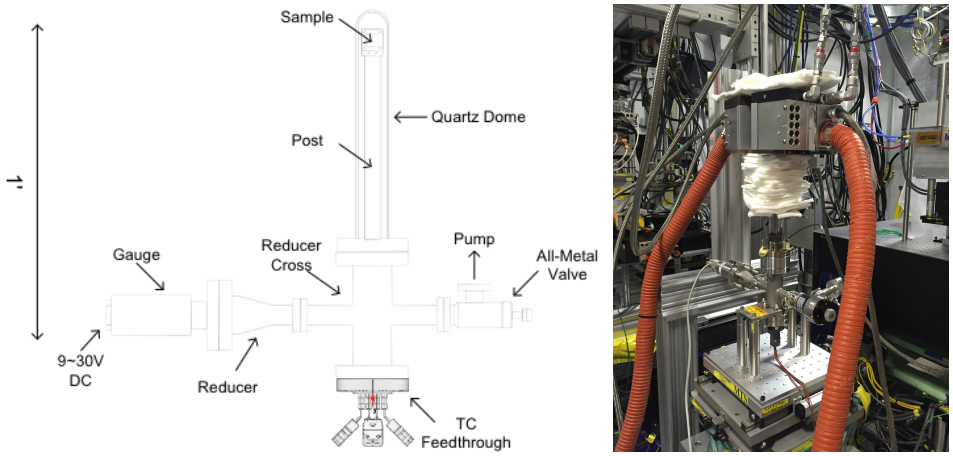

(a) (b)

Figure 2.2: Apparatus for in-situ synchrotron characterization of nuclear fuel materials: (a) overview of the design; and (b) experimental setup at the APS beamline (Hutch E, sector 1)

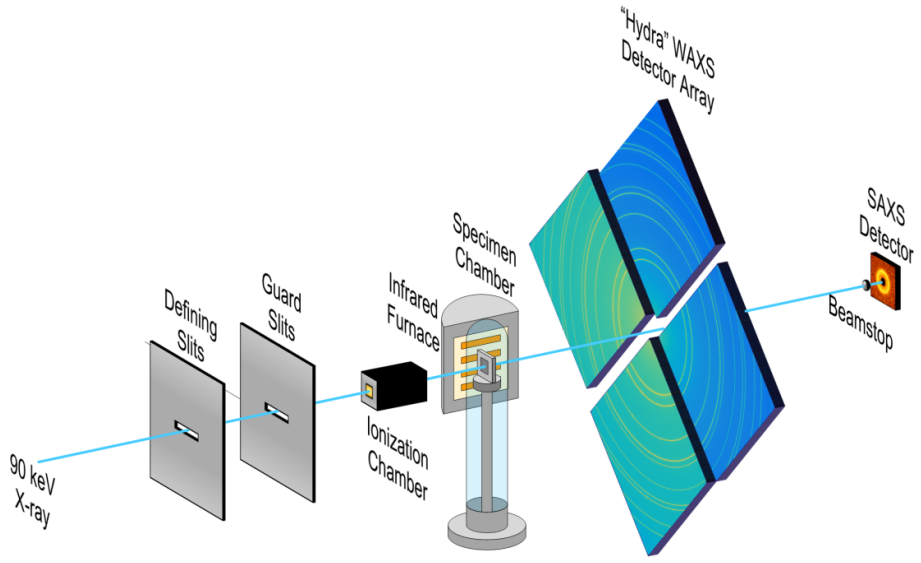

Figure 2.3: Demonstration of the experiment setup of the synchrotron X-ray investigation

During isothermal annealing of the UO_2 sample, the X-ray continuously illuminates the sample to real-time characterize the dynamics of grain growth in the UO_2 sample (Fig. 2.3). Diffraction measurements were performed with a monochromatic 90 kev X-ray beam with a beam size of 50×50 μm^2. The experiment took X-ray diffraction measurements using the "Hydra" detector array, which consists of four area detectors (GE 41RT). The distance between the sample and the detector was approximately 2.420 m. A similar experimental setup can be found in the studies in Refs. [4-8].

2.2 Art of Synchrotron Scattering Data Analysis

The WAXS data from a polycrystalline specimen contains a set of information about its microstructural characteristics. The most fundamental information that can be obtained is the spacings of atomic layers, namely, the d-spacings. The d-spacings correspond directly to the positions of the diffraction peaks in the WAXS spectrum. According to Bragg's law,

$$2d_{hkl}sin\theta_{hkl} = \lambda,$$

where λ is the wavelength of the monochromatic X-ray photons, θ is the diffraction angle, d is the d-spacing of a specific atomic layer, and the subscript $\{hkl\}$ is the Miller's index of that atomic layer. In cubic structure materials such as our material of interest, UO_2, the d-spacing of a specific reflection $\{hkl\}$ can be related to the lattice constant, a_0, through the following equation:

$$d_{hkl} = \frac{a_0}{\sqrt{h^2+k^2+l^2}},$$

Therefore, the lattice constant of the specimen can be straightforwardly measured according to the position of the diffraction peaks collected in WAXS investigations.

As the Hydra detector array is capable of collecting a full 360° azimuth angle of diffraction information, a 10° azimuth interval was selected to fit the diffraction peaks. The pseudo-Voigt peak function was assumed for the peak fitting. For each reflection, the measured d-spacing value was averaged as described by the following equation,

$$\overline{d_{hkl}} = \frac{\sum_j I^j_{hkl} d^j_{hkl}}{\sum_j I^j_{hkl}},$$

where the superscript j is the index of different azimuth interval, I_{hkl}^{j} is the integrated intensity of the $\{hkl\}$ reflection within that azimuth interval. The final lattice constant value was thereafter averaged over 10 reflections with the lowest Miller indices.

Aside from the lattice spacing information discussed above, the WAXS data also includes information about the internal strain and grain size. The interpretation of those properties, however, requires more complex processing of the broadening of diffraction peaks. One conventional approach that differentiates the grain size and internal strain contributions to peak broadening is called the Williamson-Hall (W-H) analysis. The contributions to peak breadth due to grain size and internal strain have different dependencies on the diffraction angle. In the simplified W-H analysis, it is assumed that the overall broadening of a peak is a simple sum of the size and strain broadening contributions, and the relationship can be described as:

$$\beta cos\theta = C\varepsilon sin\theta + K\lambda/D,$$

where β is the breadth of a specific reflection peak, θ is the diffraction angle, ε is the internal strain, λ is the wavelength of the photon, D is the grain size, C and K are adjustable constants.

However, the internal strain ε can originate from different sources. Strains from various origins may influence the peak broadening through different mechanisms. That is, the linear assumption in the W-H analysis is likely to be unrealistic in some cases. For instance, when the internal strain is dominated by isotropically and uniformly-distributed dislocations or dislocation loops, the W-H analysis is no longer the best interpretation of the peak broadening. Instead, Ungar et al. modified the W-H method so as to adapt it to the situation described above. In the modified W-H analysis, the dislocation density within the X-ray-illuminated volume can be measured [9]:

$$\Delta K = \frac{0.9}{D} + \left(\frac{\pi A^2 b^2}{2}\right)^{\frac{1}{2}} \rho^{\frac{1}{2}} (K\overline{C}^{\frac{1}{2}}),$$

where A is an adjustable parameter ranging from 1 to 2 for dislocation density between 10^{14} to 10^{15} m^{-2} levels, b is the length of the Burgers vector, ρ is the dislocation density, $\overline{C}$ is the contrast factor, $K = 2sin\theta/\lambda$, and $\Delta K = 2cos\theta\Delta\theta/\lambda$. $\overline{C}$ is determined by the crystal structure and stiffness tensor of the material. The stiffness tensor of UO_2 at different temperatures has been measured by inelastic neutron scattering at various temperatures [10]. As preliminary studies showed that the modified W-H method produces more accurate interpretation of the peak broadening information, only the modified method was used in this report.

The pseudo-Voigt function that was used for peak fitting has two components:

$$pV(2\theta) = I_0[\eta L(2\theta) + (1-\eta)G(2\theta)],$$

where I_0 is the peak intensity, $L(2\theta)$ is the Lorentzian component, $G(2\theta)$ is the Gaussian component, and η is the weight of the Lorentzian component. The breadth of the peak then has the following form:

$$\beta = \Delta\theta = \omega[\pi\eta + (1-\eta)\left(\frac{\pi}{ln2}\right)^{\frac{1}{2}}],$$

where ω is the half of the peak's FWHM. The instrumentation broadening that is measured by a powder ceria specimen must be eliminated from the measured peak broadening before completing this analysis. The values of $\overline{C}$ for edge ($\overline{C_e}$) and screw ($\overline{C_s}$) dislocations are different. This difference can be utilized to quantify the fraction of the screw dislocations, ν_s, and, more importantly, improve the confidence of the modified W-H fitting. To do this, two parameters of $\overline{C}$ need to be averaged separately as suggested by Ungar et al.[11]:

$$\overline{C} = \overline{C}_{h00}(1 - qH^2),$$

where $\overline{C}_{h00}$ is the average contrast factor of $\{h00\}$ reflections, q is a material characteristic parameter, and $H^2 = (h^2k^2 + h^2l^2 + k^2l^2)/(h^2 + k^2 + l^2)^2$ is a reflection parameter. Assuming both edge and screw dislocations exist in the crystal, $\overline{C}$ has the following expression:

$$\overline{C} = [v_s\overline{C}_{h00,s} + (1 - v_s)\overline{C}_{h00,e}\{1 - [v_s q_s + (1 - v_s)q_e]H^2\},$$

The v_s that maximizes the coefficient of determination (R^2) when fitting the modified W-H equation was regarded as the optimized fraction of screw dislocations in the specimen. The specific parameters that were used to calculate the contrast factors at room temperature are listed in Table 2. At elevated temperatures up to 2000 K, Hutchings's data were used to fit the stiffness tensor as a function of thermodynamics temperature[10]:

$$\begin{cases} c_{11} = -0.0778T + 413.01\ (GPa) \\ c_{44} = -0.0155T + 128.05\ (GPa) \\ c_{12} = -0.0155T + 128.05\ (GPa) \end{cases}$$

The corresponding contrast factors at various temperatures can be derived accordingly. Considering the interference from the instrument broadening, the upper limit of the grain size that can be measured by the synchrotron setup at Sector 1-ID-E is approximately 250 nm. Thus, it is a powerful tool to investigate the grain growth behavior of samples with a grain size lower than 250 nm.

Table 2.1 Parameters used in the calculation of contrast factors (room temperature)

Parameter	Values (r.t.)
c_{11}	389.3 GPa[10]
c_{12}	118.7 GPa[10]
c_{44}	59.7 GPa[10]
$A=2c_{44}/(c_{11}-c_{12})$	0.44124
c_{12}/c_{44}	1.98827
$\overline{C}_{h00,s}$	0.1143
$\overline{C}_{h00,e}$	0.1298
q_s	-0.6798
q_e	-1.8121

2.3 Results and Discussion

2.3.1 Diffraction Peaks of UO_2

The WAXS data collected by 2D detectors were first azimuthally integrated to provide a relationship between intensity and diffraction angle, or d-spacing, as shown in Fig. 2.4. The results are consistent with the previous data collected by conventional XRD. Only UO_2 single phase was identified in the as-received sample. The Ni peaks were contributed by the Ni foils used to seal the samples. After annealing at 730 °C and 820 °C, the fluorite structure UO_2 remains stable. Since the {331} reflection of UO_2 is very close to the {220} reflection of Ni, this UO_2 reflection was not used in the modified W-H fitting. Thus, 8 reflections of UO_2 were taken into account in the modified W-H fitting, which are {111}, {200}, {220}, {311}, {222}, {400}, {420}, and {422}.

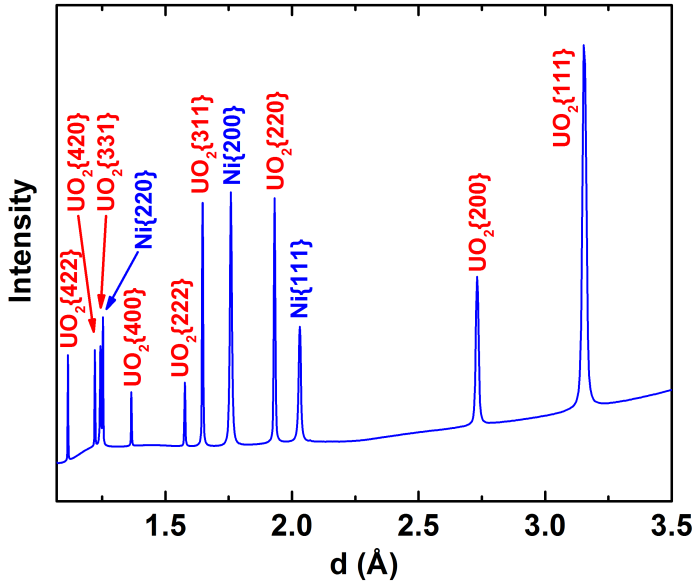

Figure 2.4: Lineout of WAXS scattering results of the as-received UO_2 sample

2.3.2 The Modified Williamson-Hall Analysis on Grain Growth

The modified W-H analysis was utilized to measure the in situ grain growth of the nano-grained UO_2 sample at 730 °C and 820 °C. Figure 2.5 shows the grain size evolution in UO_2 samples tested at 730 °C and 820 °C. Before heating, the as-received grain size was determined to be 145 nm. At 820 °C, the grain size increases rapidly until it saturates at approximately 180 nm after around 2 hours. Then the grain growth is almost negligible. On the other hand, at 730 °C, the grain growth is insignificant: the grain size only increases by 3 nm after 7.5 hours, while the saturation phenomenon also occurs at around 2 hours. To better evaluate and understand the in situ results from synchrotron scattering, the heated samples were cracked to unveil their intergranular fracture surface so that SEM can be used to measure the grain size, as shown in Figs. 2.6 and 2.7.

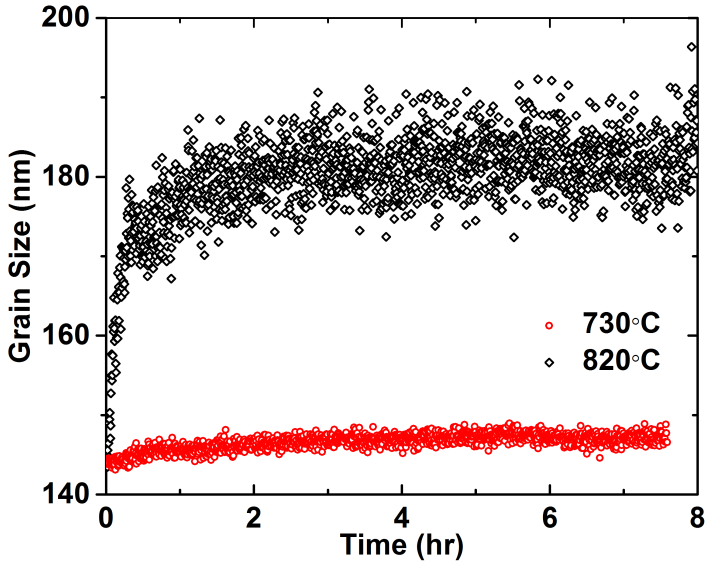

Figure 2.5 Grain size evolution in UO_2 samples heated at 730 °C and 820 °C

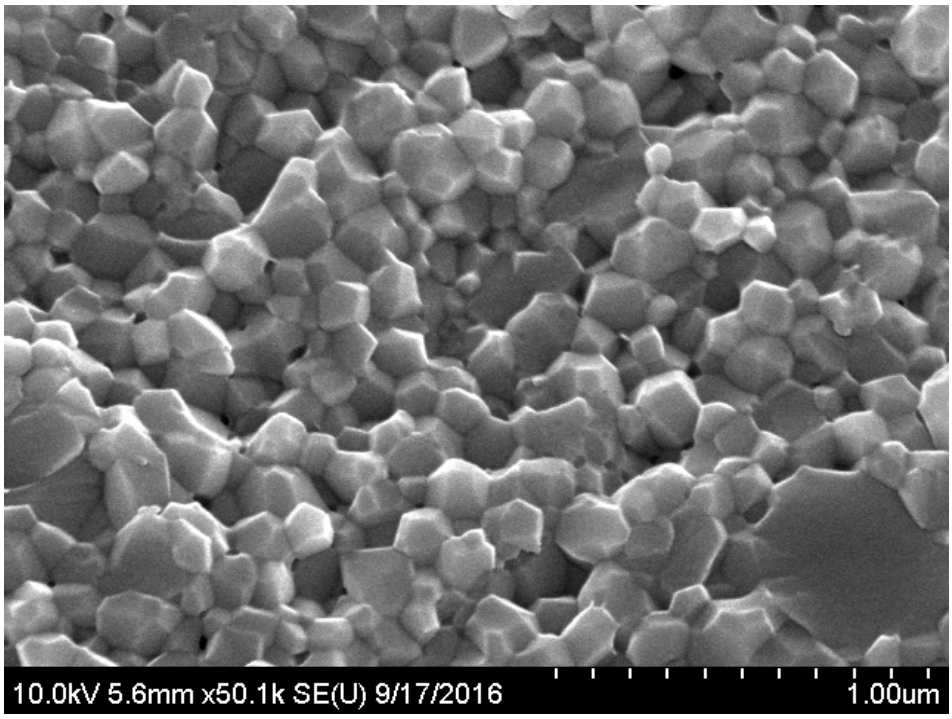

Figure 2.6 Fracture surface of the nano-grained UO_2 sample after annealing at 730 °C for 7.5 hours

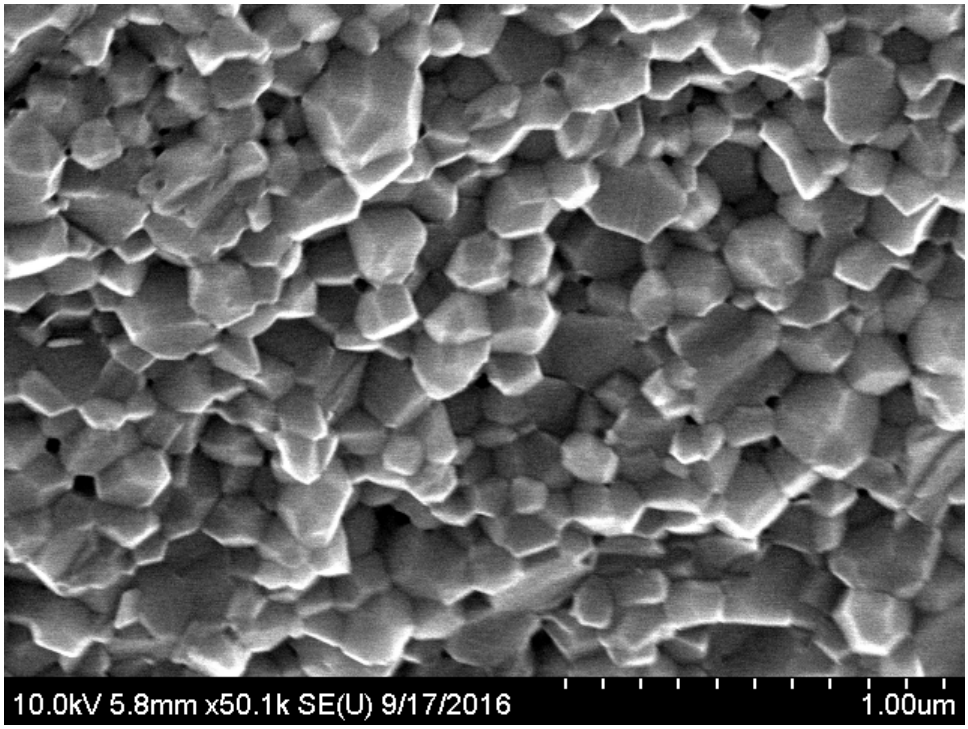

Figure 2.7 Fracture surface of the nano-grained UO_2 sample after annealing at 820 °C for 7.5 hours

The grain sizes of the two heated samples are respectively 127 ± 5 nm for 730°C and 148 ± 7 nm for 820°C. It is noticeable that the synchrotron measured grain sizes are always larger than those measured from SEM images. It is worth mentioning that the SEM measurement is actually a 2D measurement which only focuses on a surface, whereas the synchrotron technique measures the 3D grain size. Assume spherical grain shape, the 3D and 2D grain sizes differentiate by a factor of $\sqrt{3/2}$, or approximately 1.22. The ratios between the SEM and synchrotron measured grain sizes are shown in Table 2.2. The difference between the synchrotron and SEM measured sizes can be explained by this 2D/3D theory. Therefore, the two measurements are consistent.

Table 2.2 Comparison between the SEM and synchrotron measured grain sizes

	W-H analysis	SEM	Ratio
As-received	145 nm	120 ± 5 nm	1.21
730°C heated	148 nm	127 ± 5 nm	1.17
820°C heated	180 nm	148 ± 7 nm	1.22

The stagnation of grain growth after a couple of hours can be explained by the elimination of high-mobility grain boundaries [12]. In nano-grained materials sintered at 700°C, only those grain boundaries with high mobility at 700 °C were eliminated during sintering. As the sample is heated to a higher temperature, more grain boundaries are activated and become mobile, leading to rapid grain growth. Once those high-mobility grain boundaries are drained, the grain growth becomes saturated. As the nano-grained UO_2 specimen was sintered at 700 °C, the 730°C heating temperature can activate few grain boundaries, which explained the negligible grain growth at this temperature.

3. Surface Faceting in UO_2

Surface properties of UO_2 play an important role throughout the lifetime of this widely-used commercial nuclear fuel material, from manufacturing to storage. The surface features and corresponding thermodynamic characteristics influence the morphology, size, and distribution of fission gas bubbles as well as the initiation and propagation of micro-fractures within the nuclear fuel pellets. Hence, a better understanding of the surface behavior of UO_2 will help interpret the in-pile behavior of UO_2, thereby advancing the capability of precisely predicting fuel performance [13-15]. Like many other materials, the surface energy of UO_2 varies substantially with crystallographic orientation. This energy variation creates anisotropy in surface energy, which leads to the formation of surface faceting features during annealing. Detailed understanding of these orientation-dependent surface faceting features can not only expand the fundamental knowledge of the surface characteristics of UO_2, but can also shine a light on the mechanisms involved in gas swelling and micro-fracture of UO_2 fuel [16, 17]. Additionally, by establishing a deterministic correlation between the crystallographic orientation and surface morphology, it is possible to develop a method to deduce the lattice orientation of surface grains of a UO_2 sample based on its surface faceting features.

As a consequence of anisotropic surface energy, the surface faceting phenomenon occurs in a great number of crystalline materials. The surface faceting features can also be correlated with the Wulff shape of the crystal[18]. The formation mechanism for surface faceting has been investigated by both experimental and computational approaches[19-22]. Previously, the surface faceting of UO_2 was investigated by low energy electron diffraction (LEED). However, as LEED is limited to the characterization of single crystal specimens, only those planes with low Miller indices; namely, {100}, {110}, and {111} planes; have been examined[23-26]. As the closest packed layer, the {111} surface of UO_2 has the lowest surface energy[27, 28] and is, therefore, not subject to surface coarsening or faceting[29]. On the contrary, the {110} surface forms a wavy structure consisting of two {111} planes sharing a <110> edge with the angle of 109.47° as a result of annealing. In addition, although the majority of the {100} surface remains smooth during annealing, hemi-octahedra (square pyramids) that contain four {111} planes, form on the {100} surface. These pyramid features are believed to be due to the deposition of UO_2 vapor, which is generated during annealing. Only {111} and {100} planes are present at equilibrium, while the {110} and higher-index planes are absent. All the edges present on equilibrium UO_2 surfaces are <110> type, as reported by previous studies[26]. The dominance of the {111} and {100} planes and the <110> edge is also comparable to previous studies of the morphology of UO_2 single crystal. Theoretical prediction gives a simple {111} faceted octahedron[27]. Meanwhile, the experimental examination is limited to some SEM observation of voids on UO_2 surfaces, which shows a {111} faceted octahedron truncated by {100} planes[30, 31]. The appearance of {100} planes might be explained by non-equilibrium kinetics model[27] or the modification of surface energy due to hydroxidation[32, 33]. Hence, further studies are necessary to clarify the morphology of UO_2 crystal. Recently, the {100} and {111} surfaces were characterized by scanning tunneling microscopy (STM), revealing the atomic level structure of these low-index crystallographic planes[34, 35].

All previous investigations on the surface faceting features of UO_2 are limited to three low Miller index planes present within single crystal specimens. There is a scarcity of comprehensive studies on the faceting features of surfaces with general indices. In order to develop a comprehensive understanding of the faceting behavior of polycrystalline UO_2, two key properties need to be determined: the crystallographic orientation of the grains, and a quantitative description of their corresponding surface faceting features. The coarse surface of UO_2 with faceting features limits the utilization of conventional techniques. For instance, although electron backscattering diffraction (EBSD) is capable of working with coarse surfaces, the faceting features may create shadows on investigated surfaces, preventing the collection of grain to grain matching maps of crystallographic orientation, especially when grains are small. However, synchrotron X-ray diffraction is barely influenced by surface roughness due to the deep penetration ability originating from its high energy and intensity, making it an ideal technique for this study. This synchrotron technique has been adopted to examine a variety of bulk materials, including advanced Fe-based alloys[4, 5, 7, 8, 36, 37] and metallic nuclear fuel materials [38] and [39].

When the X-ray beam is focused to a submicron size, mapping of a micrograined specimen can be easily achieved[40]. Thus, synchrotron Laue microdiffraction[41] has the unique non-destructive capability of measuring the crystallographic orientation of grains with coarse surfaces. The surface features can be characterized by secondary electron (SE) imaging with SEM. Synchrotron microdiffraction and SE SEM techniques were coordinated in this study to establish the precise correlation between crystallographic orientation and the surface faceting features of multiple grains within a polycrystalline UO_2 specimen.

3.1 Experiment

3.1.1 Specimen preparation

The polycrystalline UO_2 specimen investigated in this study was fabricated utilizing spark plasma sintering (SPS) [42]. UO_2 powder was procured from International Bio-analytical Industries Inc. To reduce the particle size, the powders were ball milled for 30 min utilizing tungsten carbide container and milling balls. To produce bulk UO_2 samples, an SPS within an industrial argon atmosphere (<5 ppm oxygen) was used. The temperature was increased to 1600 °C with a 100 °C/min ramp rate, while the pressure was increased from a 10 MPa pre-load to 40 MPa. The sample was sintered for 5 min under these conditions, and then the temperature was decreased to 1500 °C at 20 °C/min as the pressure was decreased to 10 MPa. The sample was annealed for 30 min under these conditions in order to relieve residual stresses induced during sintering. The power was turned off, and the sample was allowed to cool to room temperature. Further details about the ball milling and SPS procedures can be found in Ref. [42]. The sintered UO_2 sample was mechanically polished down to 0.5 μm roughness using diamond lapping films to produce a uniformly smooth surface finish. The sample was then thermally etched by annealing at 1500 °C for 1 h in a He gas environment to activate the formation of surface faceting by enhancing surface diffusion. By measuring the lattice parameter using an PANalytical X-ray diffractometer, the stoichiometry of the sample was determined according to the following equation: $a = 5.4705 - 0.132x$[43, 44], where a is the derived lattice parameter, and x is the stoichiometry parameter as in the formula UO_{2+x}. The stoichiometry of the sample investigated in this study was found to be $UO_{2.00047 \pm 0.00608}$. No distinguishable oxygen pickup was detected during the thermal etching procedure based on the lattice parameter measurement.

3.1.2 Synchrotron microdiffraction

Synchrotron Laue microdiffraction measurements were performed at Sector 34-ID-E at the Advanced Photon Source (APS), Argonne National Laboratory (ANL). The synchrotron experiment setup is illustrated in Fig. 3.1(a). The UO_2 specimen was kept in a sealed container with a Kapton film window. The synchrotron white X-ray beam was focused by a Kirkpatrick-Baez (K-B) mirror system to provide a 0.6 μm × 0.8 μm beam size for 2D scanning. The sample was oriented such that the sample surface was at a 45° angle to the beam direction. Laue diffraction patterns were collected by a 2048 × 2048 2D area detector at an array of points across the sample. The Laue patterns were then processed to determine the reciprocal lattice vectors so that the crystal orientation of all the scanned positions could be derived. The scanning step length in both directions was 2 μm. Because the grain size of the UO_2 sample was 18.93 ± 1.28 μm according to the SEM images, approximately 70 data points were collected for each grain.

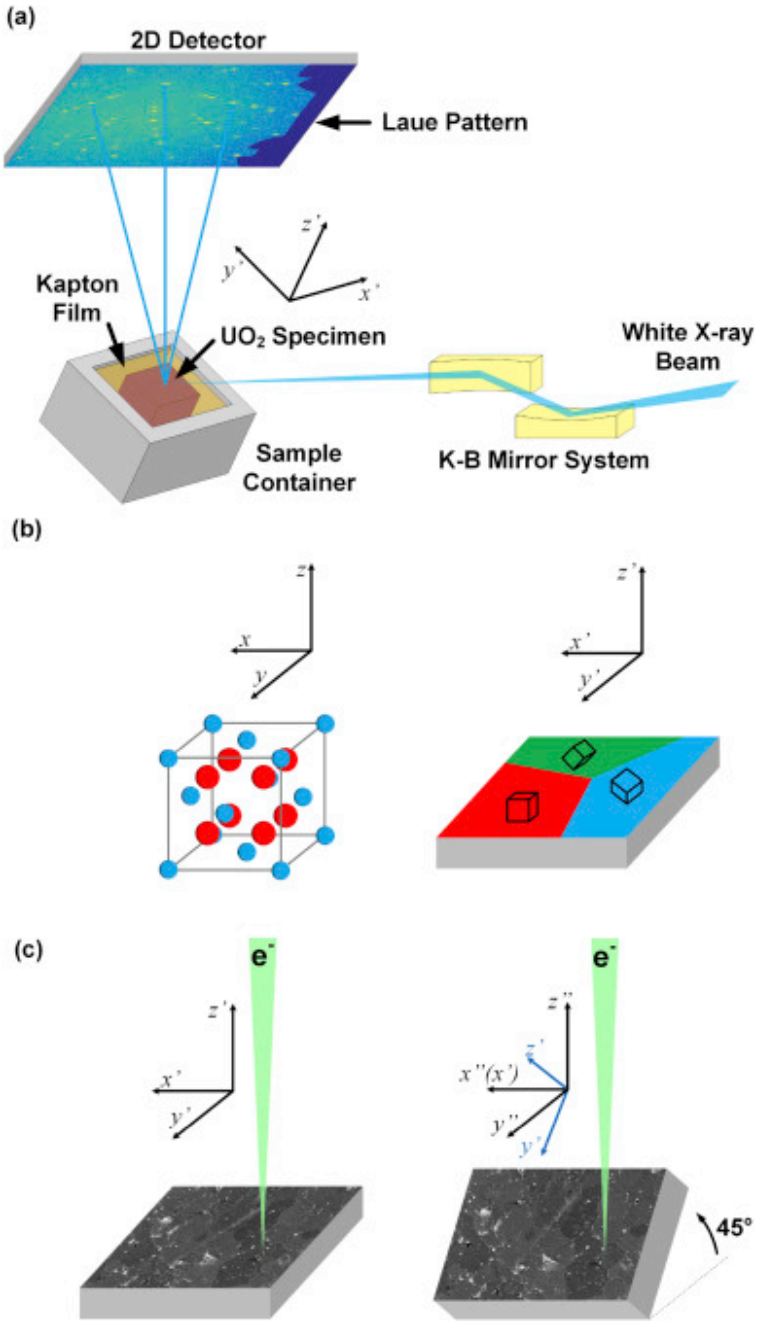

Figure 3.1 The experiment setups: (a) the setup of the synchrotron Laue microdiffraction experiment; (b) the relationship between the lattice coordinate system of UO_2 with fluorite structure (left) and the specimen coordinate system (right): each grain in the specimen has its own lattice coordination system and corresponding Euler angles for transformation to the specimen coordinate system; (c) the tilting setup of the SEM investigations: the specimen coordinate system (′) and tilted specimen coordinate system (″) are shown in this figure: the z' direction is the surface normal.

3.1.3 Surface analysis

The surface morphology of the UO_2 specimen was captured by a Hitachi S-3000N SEM. As the SEM only captures 2D projections of 3D surface features, the specimen was tilted to two angles (0° and 45°) for the regions of interest, to avert the loss of information during projection, as shown in Fig. 3.1(c). The tilting axis is the x-axis of the specimen coordination system .

Previous investigations on both surface faceting and morphology of UO_2 at equilibrium showed the dominance of {111} planes as well as the coexistence of {100} planes. However, {110} surfaces, and surfaces with higher Miller indices were not observed at equilibrium [26]. Therefore, the {111} and {100} planes are assumed to be the dominant surface facets for analysis in this study, namely, all the edges observed are assumed to be <110> type.

Any orientation of a UO_2 lattice can be described by three Euler angles: ϕ, θ and ψ, representing three rotation operations, respectively. Any point in the lattice coordinate system, $P = [x,y,z]^T$, can be transformed into the corresponding coordinates in the specimen coordinate system, P′=T[x′,y′,z′]P′=[x′,y′,z′] through the Euler rotations described by the following expression (*x*-convention)

$$P' = \begin{pmatrix} cos\psi & sin\psi & 0 \\ -sin\psi & cos\psi & 0 \\ 0 & 0 & 1 \end{pmatrix} \begin{pmatrix} 1 & 0 & 0 \\ 0 & cos\theta & sin\theta \\ 0 & -sin\theta & cos\theta \end{pmatrix} \begin{pmatrix} cos\phi & sin\phi & 0 \\ -sin\phi & cos\phi & 0 \\ 0 & 0 & 1 \end{pmatrix} P$$

Because the specimen was also tilted to 45° in SEM, the coordinate of the point in the tilted specimen coordinate system (45°), P″=[x″,y″,z″]T experiences an extra rotation operation:

$$P'' = \begin{pmatrix} 1 & 0 & 0 \\ 0 & \frac{1}{\sqrt{2}} & -\frac{1}{\sqrt{2}} \\ 0 & \frac{1}{\sqrt{2}} & \frac{1}{\sqrt{2}} \end{pmatrix} P'$$

3.2 Results

3.2.1 Orientation-dependent surface faceting

An approximately 250 μm × 400 μm region of the polycrystalline UO_2 specimen was selected to perform both Laue microdiffraction and SEM measurements (Fig. 3.2). The orientation map with inverse pole figure (IPF) coloring from the Laue microdiffraction patterns was compared to the surface topography images obtained by the SEM. Grain to grain matching between the two images confirmed that both techniques captured the same region on the specimen. Based on the orientation information obtained by microdiffraction, the surface faceting features can be correlated to the crystallographic orientation of each individual grain.

The presence of surfaces with low Miller indices ({100}, {110} and {111}) that were observed in previous studies was confirmed. Due to the unique nature of this study, a much broader range of surface normal orientations were able to be observed. The unique surface features of these orientations were mapped out on the standard stereographic triangle (SST), and are described in the following paragraph. Fig. 3.3 elucidates the change in surface morphology as the surface normal changes from <001> to <111>, along a <110> axis (on side of the SST). When the surface normal is near <001>, the surface is dominated by a {100} plane with a series of hemi-octahedra made of four {111} planes (see the blue

point in Fig. 3.3). The large pyramids sometimes are truncated by a {100} plane to form a frustum. When the surface normal is slightly inclined from <001>, the pyramids are also inclined, and the surface becomes stepped by {111} planes (see the green point in Fig. 3.3). As the surface normal becomes closer to <111>, the fraction of {111} planes increases. When the surface normal is close to <111>, the surface is dominated by a {111} plane, with steps formed by a {100} plane, and residual inclined pyramids or frusta(see the red point in Fig. 3.3). When the surface normal is perfectly <111>, it is theoretically a smooth {111} plane.

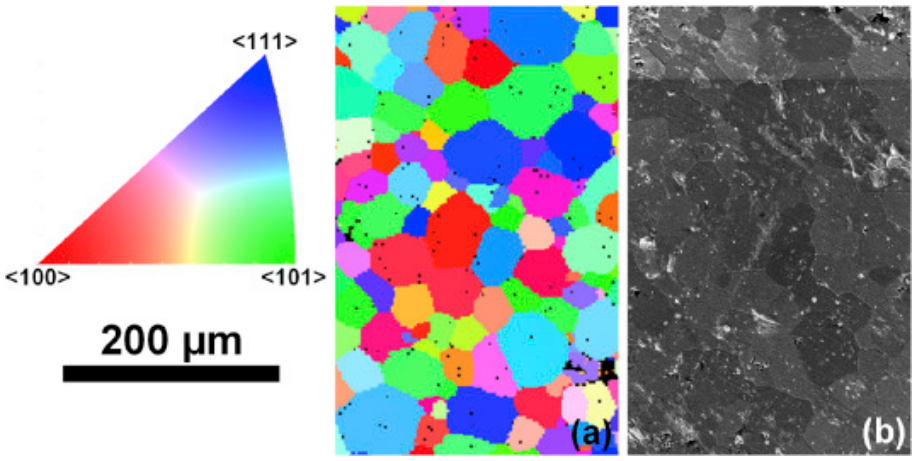

Figure 3.2 Same region in the UO_2 specimen characterized by synchrotron Laue microdiffraction and SEM: (a) orientation map determined by Laue microdiffraction patterns with inverse pole figure (IPF) coloring. The black spots represent those positions of which crystallographic orientations failed to be indexed; (b) SEM secondary electron image.

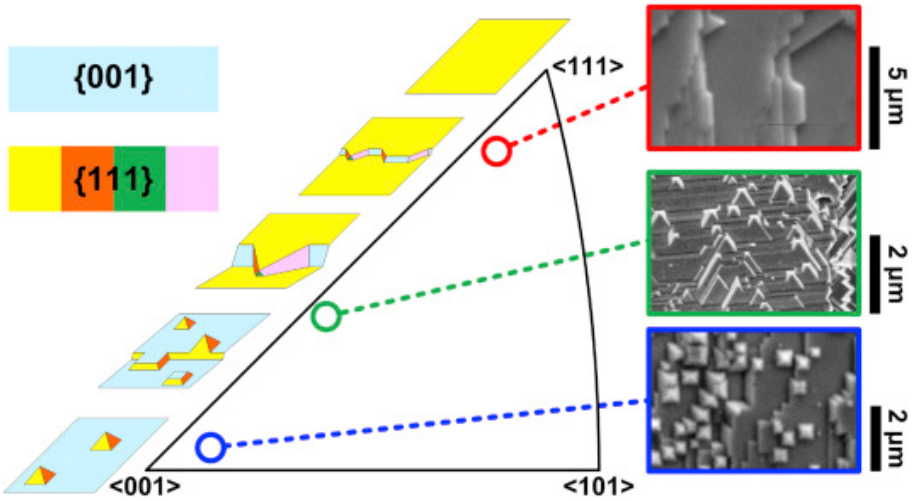

Figure 3.3 Surface faceting features with surface normal from <100> tilting to <111>: surface morphology was illustrated by both schematics and SEM images on the SST.

Fig. 3.4 shows the evolution of the surface morphology as the surface normal evolves from <001> to <101> along a <010> axis. When the surface normal is near <001>, the dominant feature is still a stepped {100} plane with {111} square pyramids or frusta. However, as the surface normal tilts towards <101>, the steps are no longer dominated by one {111} plane (as occurred when the surface normal was tilted towards <111>), but split between two {111} planes (see the red point in Fig. 3.4). As the surface normal approaches <101>, the proportion of the two {111} planes continues to increase, as

illustrated by the green and blue points in Fig. 3.4. When the surface normal is close to <101>, the surface is dominated by a wavy feature containing two {111} planes and stepped by a {100} plane (see the orange point in Fig. 3.4).

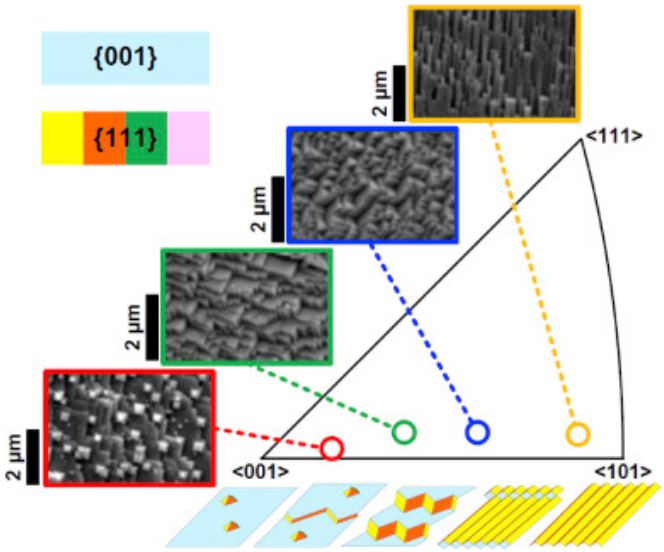

Figure 3.4 Surface faceting features with surface normal from <100> tilting to <110>: surface morphology was illustrated by both schematics and SEM images on the SST.

Fig. 3.5 tracks the surface morphology as the surface normal changes from <111> to <101> along a $<\bar{1}01>$ axis. As the surface normal tilts from <111> to <101>, the original {111} plane starts to be stepped by another {111} plane with a 107.49° angle. When the surface normal is close to <101>, the fractions of the two types of {111} planes are equal, creating the characteristic wavy features of the {110} surface. It is worth mentioning that the {100} planes are present in the SEM images in Fig. 3.5 because the surface normal is not exactly on the side.

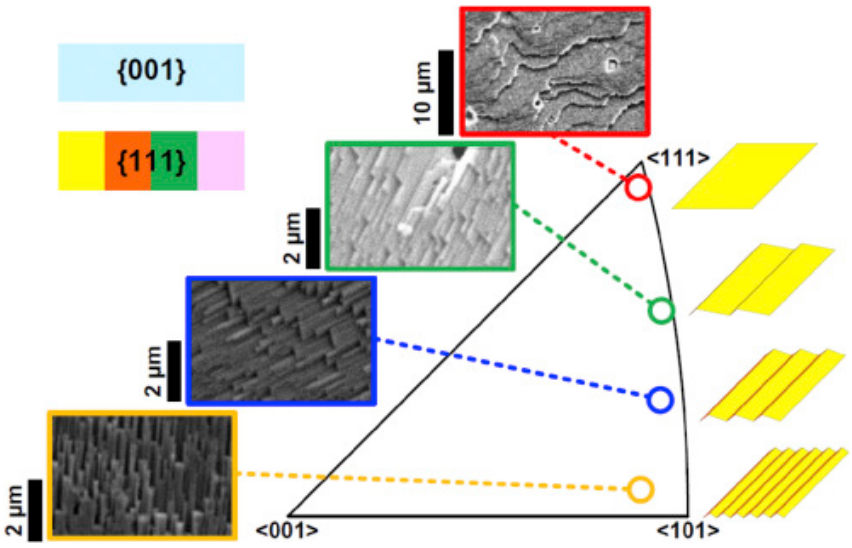

Figure 3.5 Surface faceting features with surface normal from <111> tilting to <110>: surface morphology was illustrated by both schematics and SEM images on the SST.

After investigating the surface faceting features near the three vertexes and along the three boundaries of the SST, regions with a surface normal falling in the core area of the SST were also examined. Multiple surface normal vectors within this area were studied, some representative cases of which are

shown in Fig. 3.6. For all those cases, two {111} planes and one {100} plane are present with three <110> edges, forming the so-called triple-plane structure, as defined in this study. The fraction of each plane type is determined by the specific position on the SST. For example, if the surface normal is relatively close to <001>, the {100} plane is dominant (see the red point in Fig. 3.6). Similarly, if the surface normal is relatively close to <111>, a {111} plane is dominant (see the green point in Fig. 3.6), and if the surface normal is relatively close to <101>, two {111} planes are equally dominant to form a wavy feature, as shown by the blue point in Fig. 3.6.

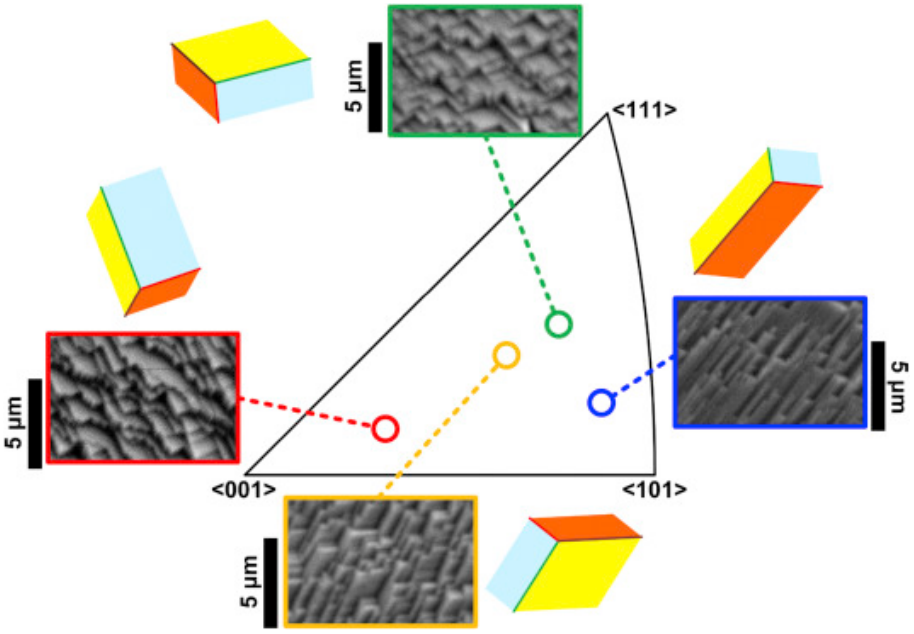

Figure 3.6 Surface faceting features with surface normal far away from the edges: surface morphology was illustrated by both schematics and SEM images on the SST.

3.3 Conclusions

In this study, synchrotron Laue microdiffraction and SEM techniques were collaboratively utilized so as to establish a general correlation between the crystallographic orientation and surface faceting features of polycrystalline UO_2. Sets of low-Miller-index planes were found across the sample, with a dependence upon the surface normal. A triple-plane structure, which contains one {100} plane, two {111} planes, and three <110> edges, is the major surface faceting feature for most orientations. The dominance of this structure can be explained by the preference in thermodynamic preference for low-energy surfaces. The coexistence of {100} and {111} planes on {100} surface also implies the variance of $\gamma_{100}/\gamma_{111}$, probably due to the local fluctuation of surface hydroxidation. The knowledge of the orientation-dependent surface faceting features was used to develop a method to determine the orientation of a grain based on SEM images. This technique is applicable for the vast majority of crystallographic orientations.

4. Fracture Toughness Measurements

In FY16, we performed nano-indentation experiments on the nano-grained and micro-grained UO_2 specimens to measure the fracture toughness. The results of experiments are reported to provide experimental data for validating the facture models used in the MARMOT-MOOSE-BISON advanced fuel performance code.

4.1 Experiments

As nano-indentation results are sensitive to the surface condition of the specimens, a series of surface processing procedures were performed to obtain a flat and smooth surface. The UO_2 samples with different grain sizes were sintered by SPS. The sample information can be found in Table 4.1. The samples were embedded in 1.25 inch diameter epoxy, and then mechanically polished by different grades of sandpapers and diamond suspensions to a 0.05 micron surface finish. The vibration polishing was further performed using a 0.05 micron diamond suspension for approximately 12 hours so as to ensure that the final surface condition was optimized for nanoindenation tests.

Table 4.1 Detailed information of the nano-grained and micro-grained UO_2 samples

Sample	Dimension (mm)	Mass (mg)	Porosity	Stoichiometry	Grain Size
Nano	2.00×2.00×0.45	9.5	3.5%	2.006 ± 0.002	123 ± 12 nm
Micro	1.70×1.10×0.50	9.8	4.2%	1.996 ± 0.004	1.8 ± 0.2 μm

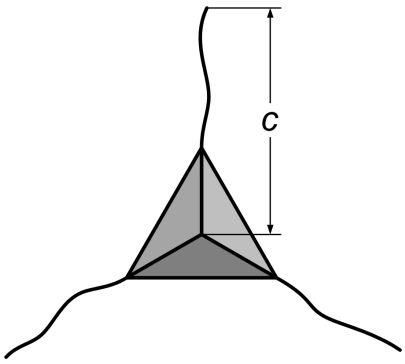

Figure 4.1 Definition of the length of the radical cracks

The nanoindentation tests were performed using a Hysitron TI 950 TriboIndentor at the Microscopy and Characterization Suite (MaCS) in the Center for Advanced Energy Studies (CAES). As a sharper indenter has a lower indentation cracking threshold, to reduce the indentation cracking threshold, a cube-corner indenter with a 35.3° symmetry-axis-to-face angle was utilized in this study instead of a conventional Berkovich indenter, which has a 65.3° symmetry-axis-to-face angle. A 5s-10s-5s loading profile was used to indent the sample. The maximum load was selected to be 200 mN. Approximately 900 indents and 200 indents were created on the sample surfaces of nano- and micro-grained UO_2 samples, respectively. The fracture toughness of both samples was derived according to the following equation [45]:

$$K_c = \alpha \left(\frac{E}{H}\right)^{1/2} \left(\frac{P}{c^{3/2}}\right)$$

Here, E is the maximum indentation load, α is an empirical constant which depends on the geometry of the indenter, E is the Young's modulus, H is the hardness, and c is the length of the radical cracks (Fig. 4.1). For a cube-corner indenter, $\alpha = 0.036$ was proved to be the appropriate value from previous studies [45]. P was selected to be 200 mN as mentioned before. E and H values were directly measured by the nano-indentation device. Finally, c was obtained by measuring the cracks of all the indents.

4.2 Results

Arrays of nanoindents were created by the nanoindenter on the surface of both UO_2 sample. Figure 4.2 shows the arrays of nanoindents on the nano-grained sample. Approximately 900 and 200 indents respectively on nano- and micro-grained UO_2 samples provide enough data for satisfactory statistics. Cracks occur at the majority of those indents, as illustrated by Fig. 4.3.

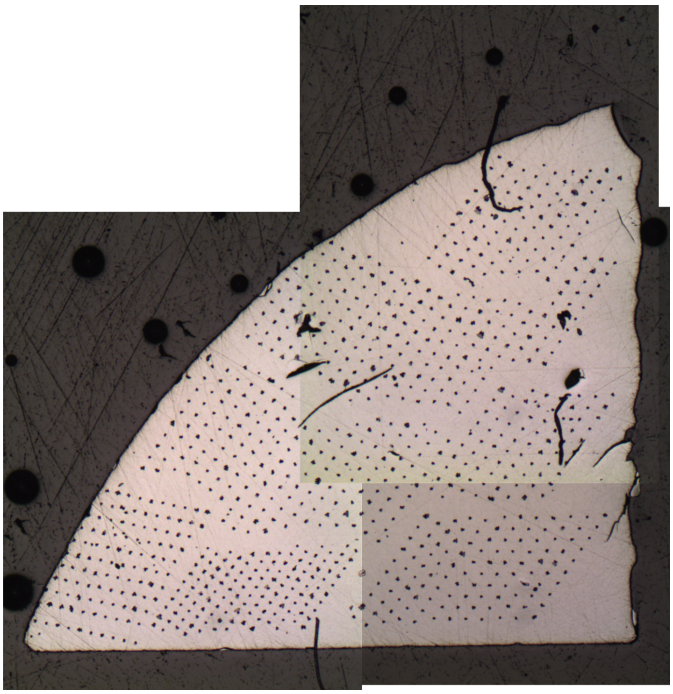

Figure 4.2 Optical microscopy image of the nano-indented surface of the nano-grained UO_2 specimen.

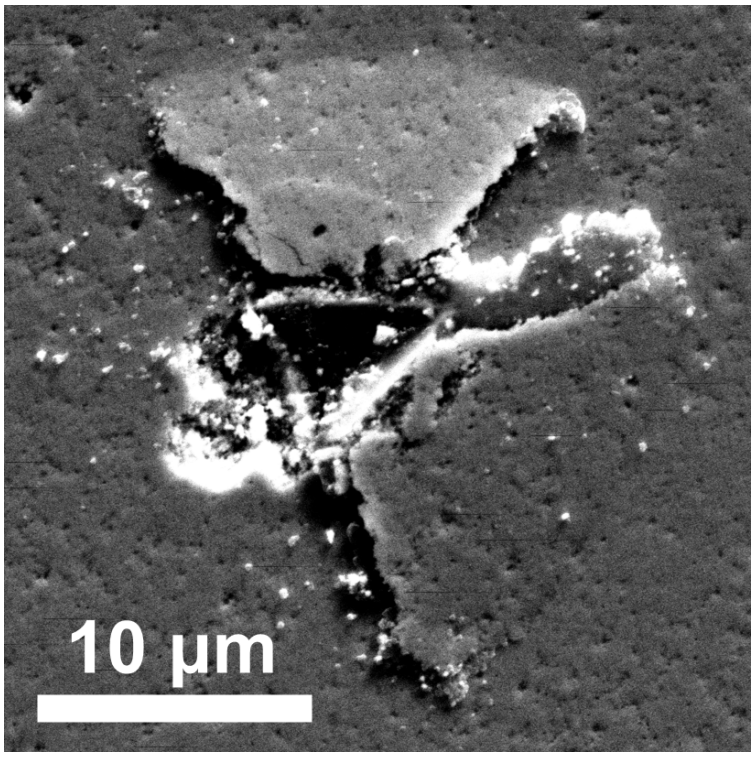

Figure 4.3 SEM image of a typical indent on the nano-grained UO_2 specimen

Table 4.2 shows the summary of the measured and derived data from nano-indentations. The measured Young's modulus of both samples are lower than the theoretical value (220 GPa), which may originate from the cracking. Thus, both measured and theoretical Young's moduli were used to calculate fracture toughness ($K_c^{measured}$ and K_c^{theroy} in Table 4.2, respectively). Both values of hardness and fracture toughness of the nano-grained UO_2 sample are lower than those of the micro-grained sample. Given the size of the voids, *a*, in the sintered UO_2 samples, the fracture stress can be further calculated by:

$$\sigma_{fracture} = K_c a^{1/2}$$

Table 4.2 Summary of the fracture toughness measurement

Sample	P(mN)	E (GPa)	H (GPa)	c (μm)	$K_c^{measured}$ (MPa·$m^{1/2}$)	K_c^{theroy} (MPa·$m^{1/2}$)
Nano	200.001±0.001	165±1	6.69±0.03	7.47±0.07	1.75±0.02	2.02±0.02
Micro	200.001±0.001	180±2	7.43±.12	5.70±0.53	2.61±0.36	2.88±0.36

5. Future Work

In FY15, we have performed several important studies on grain growth, surface morphology, and fracture toughness of UO_2 materials. The surface morphology investigation was completed. The technique developed in this study can be further applied to other experiments when using UO_2 samples in medium or large grain sizes. The other two important studies in FY16, i.e. in-situ grain growth measurements of nano-grained UO_2 materials, and fracture toughness measurements of micro-and nano-grained UO_2 materials, are the preliminary investigations, which aim to demonstrate the characterization techniques. Following the pilot works in FY16, more systematic studies will be performed to provide a set of experimental data for MARMOT validations.

The planned activities for FY17 are listed below:

1. We plan to conduct *in-situ* grain growth study of stoichiometric nano-crystalline UO_2 specimens using synchrotron X-ray diffraction. Three temperatures will be primarily studied: 800 ºC, 900 ºC, and 1000 ºC. The nano-crystalline UO_2 specimens in different porosities will be employed to investigate the impact of porosity on UO_2 grain growth behavior. If more APS beam time will be available, the *in-situ* grain growth experiment at 1100 ºC will also be conducted.
2. We plan to conduct *ex-situ* grain growth measurements of medium (3-10 microns)/large (10-30 microns) grained UO_2 specimens using SEM at different temperatures (up to 2000 ºC).
3. We plan to employ the micro-indentation technique to determine the fracture toughness/stress of UO_2 samples. UO_2 samples in three different ranges of grain size ((1) 60-500 nm; (2) 1-10 microns; & (3) 10-30 microns) will be tested. The grain-size-dependent fracture toughness/stress will be measured.

Based on the available materials by the time of experiments, the effect of stoichiometry (UO_{2+X}) may be investigated in the above experiments.

6. Summary

This activity is supported by the US Nuclear Energy Advanced Modeling and Simulation (NEAMS) Fuels Product Line (FPL) and aims at providing experimental data for validation of the mesoscale simulation code MARMOT. MARMOT is a mesoscale multiphysics code that predicts the coevolution of microstructure and properties within reactor fuel during its lifetime in the reactor. It is an important component of the Moose-Bison-Marmot (MBM) code suite developed by Idaho National Laboratory (INL) to enable next generation fuel performance modeling capability as part of the NEAMS Program FPL. In order to ensure the accuracy of the microstructure-based materials models being developed within the MARMOT code, extensive validation efforts must be carried out. In this report, we summarize our work on methodology study of the use of synchrotron X-rays to measure the grain growth of nano-grained UO_2 at various temperatures. The results were compared with the SEM measurement and show great consistence, demonstrating that synchrotron scattering can be a powerful tool to capture the kinetics of grain growth of UO_2 materials. The kinetic parameters, e.g., activation energy for grain growth for UO_2, will be obtained and compared with molecular dynamics (MD) simulation results. As the capability has been established, in FY17, this technique will be applied to UO_2 specimens with a variety of stoichiometries and grain sizes.

In addition to synchrotron grain growth investigation, the surface morphology of polycrystalline UO_2 and its correlation with the crystallographic orientation were studied by combined efforts of synchrotron Laue microdiffraction and SEM imaging. The surface faceting features of polycrystalline UO_2 have been successfully connected to the orientation of each grain. This study not only provides surface morphology information of UO_2 that can be references for UO_2 surface energy research, but also enlightened a new method that can be used to determine the crystallographic orientation of surface grains of polycrystalline UO_2 samples purely based on SEM images. The method can potentially be extended to other crystalline materials that have surface faceting phenomenon.

Additionally, the fracture toughness of UO_2 with both nanoscale and microscale grain sizes was measured by nano-indentation. A cube-corner indentation tip was selected to lower the cracking threshold. The fracture toughness of both samples was deduced from the cracking length of hundreds of indents to provide satisfactory statistics. Nano-grained UO_2 was found to have lower hardness and fracture toughness in comparison with micro-grained UO_2. The results will be used to deduce the fracture stress of UO_2, and therefore help develop and validate the related microfracture models used in the MARMOT code.

7. Acknowledgements

This work was supported under US Department of Energy Contract DE-AC02-06CH11357. We would like to thank the MARMOT development lead, Yongfeng Zhang, for providing very helpful guidance for this work. Jie Lian and Yiankai Yao acknowledged the support of the DOE Nuclear Energy University Program (NEUP) under the contract DE-NE000840.

8. References

1. Kun Mo, Yinbin Miao, Di Yun, Laura Jamison, Jie Lian, Tiankai Yao, "Synchrotron characterization of nanograined UO_2 grain growth," ANL/NE-15/25, 2015
2. Kun Mo, Yinbin Miao, Di Yun, Laura Jamison, Jie Lian, Tiankai Yao, "Supplying materials needed for grain growth characterizations of nano-grained UO_2," ANL/NE-15/27, 2015
3. "Thermophysical properties database of materials for light water reactors and heavy water reactors," IAEA-TECDOC-1496, 2006
4. Y. Miao, K. Mo, Z. Zhou, X. Liu, K. Lan, G. Zhang, M. K. Miller, K. A. Powers, J. Almer, J. F. Stubbins, "*In-situ* Synchrotron Tensile Investigations on the Phase Responses within an Oxide Dispersion-strengthened (ODS) 304 Steel," *Materials Science and Engineering: A,* Vol. 625, 146-152, 2015
5. K. Mo, Z. Zhou, Y. Miao, D. Yun, H. Tung, G. Zhang, W. Chen, J. Almer, and J. F. Stubbins, "Synchrotron study on load partitioning between ferrite/martensite and nanoparticles of a 9Cr ODS steel," *Journal of Nuclear Materials*, Vol. 455, 376–381, 2014
6. K. Mo, H. Tung, J. Almer, M. Li, X. Chen, W. Chen, J. B. Hansen, J. F. Stubbins, "Synchrotron radiation study on Alloy 617 and Alloy 230 for VHTR application," *Journal of Pressure Vessel Technology*, Vol. 135, paper No. 021502, 2013
7. G. Zhang, Z. Zhou, K. Mo, Y. Miao, X. Liu, J. Almer, J. F. Stubbins, "The evolution of internal stress and dislocation during tensile deformation in a 9Cr Ferritic/Martensitic (F/M) ODS steel investigated by high-energy X-rays," *Journal of Nuclear Materials*, Vol. 467, 50-57, 2015
8. Y. Miao, K. Mo, Z. Zhou, X. Liu, K. Lan, G. Zhang, M. K. Miller, K. A. Powers, Z. Mei, J. Park, J. Almer, J. F. Stubbins, "On the Microstructure and Strengthening Mechanism in ODS 316 Steel: A Coordinated Electron Microscopy, Atom Probe Tomography and *In-situ* Synchrotron Tensile Investigation," *Materials Science and Engineering: A*, Vol. 639, 585-596, 2015
9. T. Ungar, "Strain broadening caused by dislocations," *Materials Science Forum*, Vol. 278, 151–157, 1998
10. M. Hutchings, "High-temperature studies of UO_2 and ThO_2 using neutron scattering techniques," *J. Chem. Soc., Farady Trans. 2*, Vol. 83, 1083-1103, 1987
11. T. Ungar, I. Dragomir, A. Revesz, A. Borbely, "The contrast factors of dislocations in cubic crystals: the dislocation model of strain anisotropy in practice," *Journal of Applied Crystallography*. Vol. 32, 992–1002, 1999
12. E.A. Holm, S.M. Foiles, "How grain growth stops: a mechanism for grain-growth stagnation in pure materials," *Science*, 328, 1138-1141, 2010
13. M. Lyons, R. Boyle, J. Davies, V. Hazel, T. Rowland, "UO_2 properties affecting performance," *Nuclear Engineering and Design*, 21, 167–199, 1972
14. M. Notley, I. J. Hastings, "A microstructure-dependent model for fission product gas release and swelling in UO_2 fuel," *Nuclear Engineering and Design,* 56, 163–175, 1980
15. M. Tucker, "Grain boundary porosity and gas release in irradiated UO_2," *Radiation Effects*, 53, 251–255, 1980
16. T. Kutty, K. Chandrasekharan, J. Panakkal, J. Ghosh, "Fracture toughness and fracture surface energy of sintered uranium dioxide fuel pellets," *Journal of Materials Science Letters*, 6, 260–262, 1987
17. K. Forsberg, A. Massih, "Diffusion theory of fission gas migration in irradiated nuclear fuel UO_2," *Journal of Nuclear Materials*, 135, 140–148, 1985
18. J. W. Cahn, C. A. Handwerker, "Equilibrium geometries of anisotropic surfaces and interfaces," *Materials Science and Engineering: A*, 162, 83–95, 1993
19. W. Mullins, "Theory of linear facet growth during thermal etching," *Philos. Mag.*, 6, 1313–1341, 1961
20. E. D. Williams, N. C. Bartelt, "Surface faceting and the equilibrium crystal shape," *Ultramicroscopy*, 31, 36–48, 1989

21. E. D. Williams, N. Bartelt, "Thermodynamics of surface morphology," *Science*, 251, 393–400, 1991
22. J. R. Heffelfinger, C. B. Carter, "Mechanisms of surface faceting and coarsening," *Surface Science*, 389, 188–200, 1997
23. W. Ellis, R. Schwoebel, "LEED from surface steps on uo 2 single crystals," *Surf. Sci.*, 11, 82–98, 1968
24. W. P. Ellis, "LEED studies of uo 2 (111) vicinal surfaces," *Surface Science*, 45, 569–584, 1974
25. T. Taylor, W. Ellis, "A LEED study of UO_2 (100) vicinal surfaces," *Surface Science*, 77, 321–336, 1978
26. V. Krasevec, B. Navinsek, "Faceting of UO_2 single crystal surfaces," *Physica Status Solidi (A)*, 30, 501–509, 1975
27. M. Abramowski, R. W. Grimes, S. Owens, "Morphology of UO_2," *Journal of Nuclear Materials*, 275, 12–18, 1999
28. F. N. Skomurski, R. C. Ewing, A. L. Rohl, J. D. Gale, U. Becker, "Quantum mechanical vs. empirical potential modeling of uranium dioxide (UO_2) surfaces:(111), (110), and (100)," *American Mineralogist*, 91, 1761–1772, 2006
29. S. Dudarev, M. Castell, G. Botton, S. Savrasov, C. Muggelberg, G. Briggs, A. Sutton, D. Goddard, "Understanding STM images and EELS spectra of oxides with strongly correlated electrons: a comparison of nickel and uranium oxides," *Micron* 31, 363–372, 2000
30. W. Van Lierde, "On the surface free energy anisotropy of UO_2," *Journal of Materials Science*, 5, 527–531, 1970
31. M. R. Castell, "Wulff shape of microscopic voids in UO_2 crystals," *Physical Review B*, 68, 235411, 2003
32. A. H. Tan, M. Abramowski, R.W. Grimes, S. Owens, "Surface defect configurations on the (100) dipolar surface of UO_2," *Physical Review B*, 72, 035457, 2005
33. A. H. Tan, R. W. Grimes, S. Owens, "Structures of UO_2 and PuO_2 surfaces with hydroxide coverage," *Journal of Nuclear Materials,* 344, 13–16, 2005
34. M. Castell, C. Muggelberg, G. Briggs, D. Goddard, "Scanning tunneling microscopy of the UO_2 (111) surface," *Journal of Vacuum Science & Technology B*, 14, 966–969, 1996
35. C. Muggelberg, M. Castell, G. Briggs, D. Goddard, "An STM study of the UO_2 (001) surface," *Applied Surface Science*, 142, 124–128, 1999
36. Y. Miao, K. Mo, B. Cui, W.-Y. Chen, M.K. Miller, K.A. Powers, V. McCreary, D. Gross, J. Almer, I.M. Robertson, J.F. Stubbins, "The interfacial orientation relationship of oxide nanoparticles in a hafnium-containing oxide dispersion-strengthened austenitic stainless steel," *Mater. Charact.*, 101, 136–143, 2015
37. G. Zhang, K. Mo, Y. Miao, X. Liu, J. Almer, Z. Zhou, J.F. Stubbins, "Load partitioning between ferrite/martensite and dispersed nanoparticles of a 9cr ferritic/martensitic (F/M) ODS steel at high temperatures," *Materials Science and Engineering: A*, 637, 75–81, 2015
38. D. Brown, D. Alexander, K. Clarke, B. Clausen, M. Okuniewski, T. Sisneros, "Elastic properties of rolled uranium–10wt.% molybdenum nuclear fuel foils," *Scr. Mater.*, 69, 666–669, 2013
39. Y. Miao, K. Mo, B. Ye, L. Jamison, Z.-G. Mei, J. Gan, B. Miller, J. Madden, J.-S. Park, J. Almer, A.M. Yacout, "High-energy synchrotron study of in-pile-irradiated U–Mo fuels," *Scripta Materialia,* 114, 146–150, 2016
40. D. Yun, Y. Miao, R. Xu, Z. Mei, K. Mo, W. Mohamed, B. Ye, M. J. Pellin, A. M. Yacout, "Characterization of high energy xe ion irradiation effects in single crystal molybdenum with depth-resolved synchrotron microbeam diffraction," *Journal of Nuclear Materials*, 471, 272 – 279, 2016
41. J.-S. Chung, G. E. Ice, "Automated indexing for texture and strain measurement with broad-bandpass x-ray microbeams," *Journal of Applied Physics*, 86, 5249–5255, 1999
42. T. Yao, S. M. Scott, G. Xin, J. Lian, "TiO_2 doped UO_2 fuels sintered by spark plasma sintering," *Journal of Nuclear Materials* ,469, 251–261, 2016
43. K. Teske, H. Ullmann, D. Rettig, "Investigation of the oxygen activity of oxide fuels and fuel-

fission product systems by solid electrolyte techniques. part I: qualification and limitations of the method," *Journal of Nuclear Materials*, 116, 260–266, 1983
44. T. Wangle, V. Tyrpekl, M. Cologna, J. Somers, "Simulated UO_2 fuel containing CsI by spark plasma sintering," *Journal of Nuclear Materials,* 466, 150–153, 2015
45. D.S. Harding, W.C. Oliver, G.M. Pharr, "Cracking during nanoindenation and its use in the measurement of fracture toughness," *MRS Proceedings*, 356, 663-668, 1994

Nuclear Engineering Division
Argonne National Laboratory
9700 South Cass Avenue, Bldg. 208
Argonne, IL 60439

www.anl.gov

Argonne National Laboratory is a U.S. Department of Energy laboratory managed by UChicago Argonne, LLC